

Research Article

Broadening Band of Wind Speed for Aeroelastic Energy Scavenging of a Cylinder through Buffeting in the Wakes of a Squared Prism

Junlei Wang ¹, Linfeng Geng ¹, Meng Zhang ², Guifeng Zhao ², Min Zhang ³,
Zhien Zhang ¹ and Yaoliang Li²

¹School of Chemical Engineering and Energy, Zhengzhou University, Zhengzhou 450001, China

²School of Civil Engineering, Zhengzhou University, Zhengzhou 450001, China

³Shipping and Marine Engineering College, Chongqing Jiao Tong University, Chongqing 400054, China

Correspondence should be addressed to Meng Zhang; zhangmeng@zzu.edu.cn

Received 6 June 2018; Accepted 23 August 2018; Published 16 September 2018

Academic Editor: Md Abdul Halim Miah

Copyright © 2018 Junlei Wang et al. This is an open access article distributed under the Creative Commons Attribution License, which permits unrestricted use, distribution, and reproduction in any medium, provided the original work is properly cited.

Small-scale energy harvesting from ambient vibration induced by aerodynamic instabilities can be used for wireless sensing applications. The configuration with a bluff body attached to a piezoelectric cantilever has been exploited in many studies. For low-wind energy harvesting, vortex-induced vibration is investigated more frequently than other types of flow-induced motions, such as galloping and flutter, because of its quasisteady behavior called the potential lock-in phenomenon. In practice, a stationary square column is placed before the energy harvester to generate wake shedding, which can broaden the bandwidth of the energy harvester compared with a pure energy harvester equipped with a single bluff body. This paper presents a proposed CFD method coupled with an electromechanical model to predict the performance of the energy harvester. The proposed approach is verified with our experimental setup. The time history of the voltage output and the frequency response is obtained by performing the relevant experiments. A subsequent CFD study is performed to investigate the flow patterns of the present energy harvesting system.

1. Introduction

Recently, the development of renewable energy technology motivated the development of low-power level piezoelectric energy harvesting, which is expected to solve the issue of energy supply for small wireless sensors and micro-electromechanical system (MEMS) [1–3]. There are many ambient energy sources (including mechanical vibrations, human motions, and fluid flows) that can be harvested based on reasonable energy harvesting devices [4–8]. Vibration is a common phenomenon in the natural world. Generally, starting approximately one decade ago, the study of piezoelectric energy harvesting from vibration has become quite mature [9–12]. Many studies have been performed on harvesting energy from base vibrations using piezoelectric materials. In contrast, piezoelectric energy harvesting from

wind flow has received relatively little attention compared with energy harvesting from vibrations. Wind energy harvesting can be generally divided into flutter, galloping, and vortex-induced vibration-based energy harvesters. The flutter phenomenon occurs when the two modal resonant frequencies of torsion and bending modes coalesce with each other. Bryant and Garcia [13] originally proposed a flutter-based aeroelastic energy harvester; they found that the harvester oscillated in a limited cycle at higher wind speeds above a critical wind speed. Aquino et al. [14] modeled a flutter-based aeroelastic energy harvester using computational fluid dynamics (CFD) and experimentally obtained a peak-to-peak voltage of 8.72 V and a short-circuit current of 1 mA when subjected to a wind speed of 2.3 m/s. Galloping occurs on a flexible base supported with a bluff body. Ewere et al. [15] experimentally investigated galloping

piezoelectric energy harvesters with square bluff bodies. Yang et al. [16] experimentally investigated the influence of the bluff body shape on the energy harvesting performance of galloping piezoelectric energy harvesters. Weinstein et al. [17] tested the energy harvesting performance of a piezoelectric beam in the real heating, ventilation, and air conditioning flow. Zhang et al. [18] numerically investigated synchronization phenomenon in VIV energy harvesters. Recently, Dai et al. [19] explored the influence of a fixed cylinder on the energy harvesting performance of an aeroelastic energy harvester and experimentally verified the enhanced performance. Hobeck and Inman [20] presented a dual cantilever flutter and experimentally verified the large-amplitude vibration and high velocity of the two cantilever beams in the flutter. These results demonstrate that the dual cantilever flutter can be used to efficiently harvest energy from wind flow. However, the coupling physical phenomenon between an energy harvester and a stationary interrupting bluff body remains to be investigated. From the physical point of view, the cycled wake shedding effect of a bluff body may enhance the vibration of the harvesters and may improve the energy harvesting performance; this process is called buffeting. There exists a fundamental type of VIV called buffeting, which is caused by the unsteadiness of the incoming flow. Buffeting is also a common and widespread natural phenomenon. Natural turbulence combined with the presence of the wake of the forward bluff body induces buffeting. In aeronautics, it is crucially important to predict the threshold of the buffeting. The essential elements of buffeting are as follows: flow separation on the surface of the body, instability caused by the upstream obstacle (such as vortex shedding from other bluff bodies), and complex turbulence phenomena. Flow separation often occurs as the dynamic response of flight wings at high angles of attack. When the response of wings holds a wide frequency band of excitation, buffeting can be excited on aircrafts. As the second and most important source, the von Kármán vortex street that arises from wake oscillations behind a blunt body can directly lead to a so-called wake buffeting. Wake buffeting is a quite commonly observed phenomenon in many urban areas with many tall buildings. Wake buffeting generally contains two components of frequencies. The third source, pressure fluctuation of buffeting, can cause significant vertical and torsional motions, even at low flow speeds. Because of the three source types, buffeting can occur in a wide range of flow speeds, i.e., there is no critical onset wind velocity nor is there a limited range.

Buffeting is mostly dynamic in nature; as a result, altering the stiffness or damping of the structure will not necessarily change the fatigue load [21]. Although the amplitude of oscillation due to buffeting is typically smaller than that for VIV, the frequency range over which it can occur is greater, from 0.1 to 60 Hz [22]. Recently, it has been found that a freshly killed fish is capable of moving upstream within the Kármán vortex street generated by a D-shape cylinder [23]. Furthermore, Beal et al. showed that live fish can swim upstream without any energy of their own; they extract the required energy from the oncoming large-scale

vortices [24]. This observation is also important in the development of low-drag energy harvesting devices.

To exploit this important phenomenon in energy harvesting, the “eel” concept for energy harvesting was first presented by Allen and Smith [25]; the authors placed an array of slender PVDF under a stationary round sectioned bluff body and obtained milliwatt-level energy output. VIV-based energy harvesters efficiently work when the vortex-shedding frequency becomes nearly equal to one of the natural frequencies of the dynamical structure. In the year 2012, Akaydin et al. [26] experimentally obtained a peak power of 0.1 mW at a wind speed of 1.192 m/s. Goushcha et al. [27] explored the driving mechanisms of VIV energy harvesting by using particle image velocimetry. Despite these studies, there remains a lack of study of the performance of a VIV cylinder energy harvester placed behind a stationary bluff body producing a vortex-shedding street.

Accordingly, the present work aims to study a new configuration of buffeting energy harvesting containing a PEH and a stationary square column placed in front of the PEH. The square column was used to generate a Kármán vortex street, and the effect of different spacing between the stationary column and the VIV energy harvester was investigated. The purpose of the present study was to obtain an appropriate spacing to enhance the potential wind energy harvesting capability. Wind tunnel tests were performed to investigate the influence of the spacing between the stationary column and the VIVPEH on the voltage output and on the efficient wind speed region. To provide a complement of the wind tunnel test, CFD was conducted to analyze the vortex-shedding patterns in the vibration system.

2. Physical Model and Experimental Setup

Figure 1 shows a schematic of the proposed system; it mainly consists of one piezoelectric energy harvester with one MFC piece that can oscillate freely, as well as one stationary square column. The VIV bluff body suffers simultaneously two types of flow-induced force: the wake-induced and flow-induced forces. The square column is used to produce a vortex-shedding wake, which induces the vibration of the energy harvester. In this work, the diameter d and the length l_b of the circular cylinder are 32 mm and 125 mm, respectively, and the length of side l_s and total length L of the square column are also 32 mm and 125 mm, respectively. L is the center-to-center distance of the two bluff bodies in the equilibrium position.

3. Mathematical Model

Based on the Euler–Bernoulli beam theory, the Rayleigh–Ritz method, the assumed-modes method, the system identification, etc., the proposed harvester shown in Figure 1 has the following equivalent nonlinear electro-mechanical governing equations based on the following Erturk model [28]:

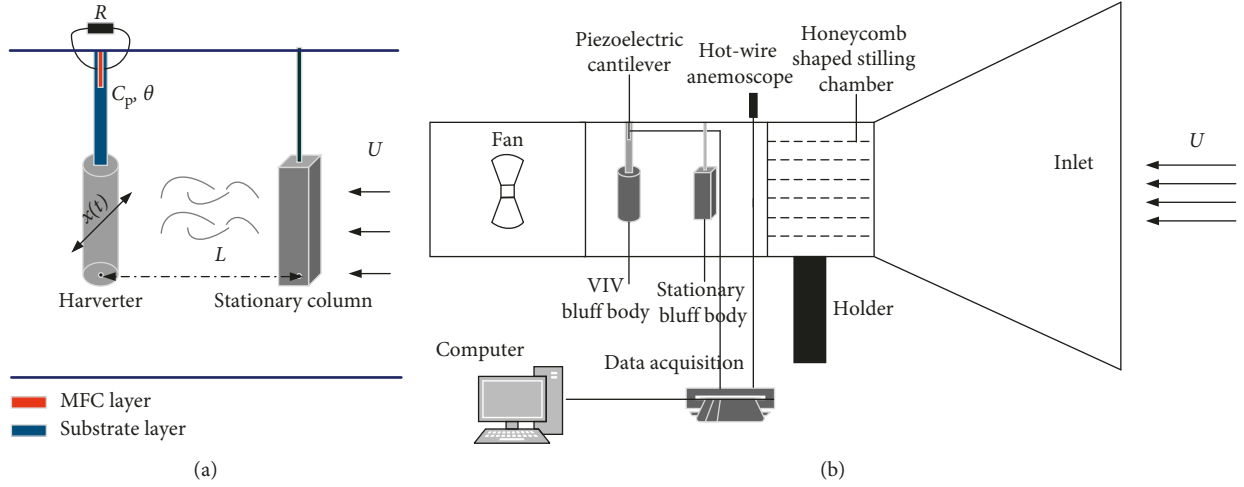


FIGURE 1: Schematic of the proposed harvester. (a) Physical system model and (b) schematic of the experimental setup.

$$\begin{aligned} M\ddot{y}(t) + C\dot{y}(t) + Ky(t) + \theta V(t) &= F_{\text{MIM}}(t) + F_{\text{EIM}}(t), \\ C_p \dot{V}(t) + V(t)R^{-1} - \theta \dot{y}(t) &= 0, \end{aligned} \quad (1)$$

where M_{eff} is the equivalent mass of a piezoelectric cantilever system; C_{eff} is the equivalent damping related to the damping coefficient ξ , which can be obtained by free decay experiments; K_{eff} is the equivalent stiffness of the system; and θ is the electromechanical coupling coefficient of the system that can be derived from equation group (2). In equation group (2), C_p is the permittivity measured experimentally, ω_n is the natural frequency of the system that can be obtained by free decay experiments, δ is the ratio of the amplitude before and after the free decay experiment, R_L is the external load of the system, and $V(t)$ is the output voltage of the system. F_{MIN} is the flow-induced force caused by the incoming wind force and F_{EIM} is the interactional force caused by the vortex shedding from the upper square column.

$$\left\{ \begin{aligned} M_{\text{eff}} &= \frac{33}{140}(m_1 + m_2) + m_3, \\ C_{\text{eff}} &= 2M_{\text{eff}}\omega_n\xi, \\ \xi &= \frac{In\delta}{\sqrt{4\pi^2 + (In\delta)^2}}, \\ K &= M_{\text{eff}}\omega_n^2, \\ \theta &= \sqrt{(\omega_{\text{on}}^2 - \omega_{\text{sn}}^2)M_{\text{eff}}C_p}. \end{aligned} \right. \quad (2)$$

In the past few decades, researchers have made a substantial effort to model the aerodynamic force of flow-induced vibration. The force of a single bluff body can be easily modeled for the vortex-induced vibration and galloping processes; however, to model the force of multiple

bluff bodies, it is difficult to objectively consider the phase difference or other time-dependent physical variables. For modeling the vortex-induced vibration force of a single bluff body, the van der Pol wake oscillator model is the most commonly used model because of its ease of understanding and its good match with the experimental results. The van der Pol wake oscillator model was first developed by Bishop and Hassan [29], Hartlen and Currie [30], Griffin et al. [31], and Skop and Griffin [32] to directly represent the body and wake oscillator equations coupled through common terms. Subsequently, to describe VIV and the lock-in phenomenon, Nayfeh [33], Facchinetti et al. [34], and Farshidianfar and Zanganeh [35] improved the traditional models. Note that all the wake oscillator models are sensitive to the coupling term introduced in the form of displacement, velocity, and acceleration. The quasisteady hypothesis is often used in modeling the galloping aerodynamic force; for example, from experimental results, the aerodynamic force of a galloping bluff body is found to be a function of the angle of attack and can be expressed as a polynomial expansion [22].

However, there is a lack of research on the modeling vortex-induced vibration between multiple bluff bodies that are either all in motion or partly in motion because it is difficult to model the force caused by the vortex-shedding street of the upper bluff body. Thus, an experimental method is the most commonly used in the relevant research studies. Unfortunately, restricting factors, such as visualization, sizing, and flow speeds, make it difficult to conduct such experiments. As a result, usually, one cannot obtain the mechanism accurately.

In this work, a numerical method was utilized to obtain the aerodynamic force, and the Gauss law was solved based on the computational results of force and the displacement from the numerical codes. The results of the Gauss law computation also influence the numerical simulations. During this process, the aero-electromechanical coupling problem was solved.

As shown in Figure 2, when the uniform flow is first combined with the vortex-shedding street of the square

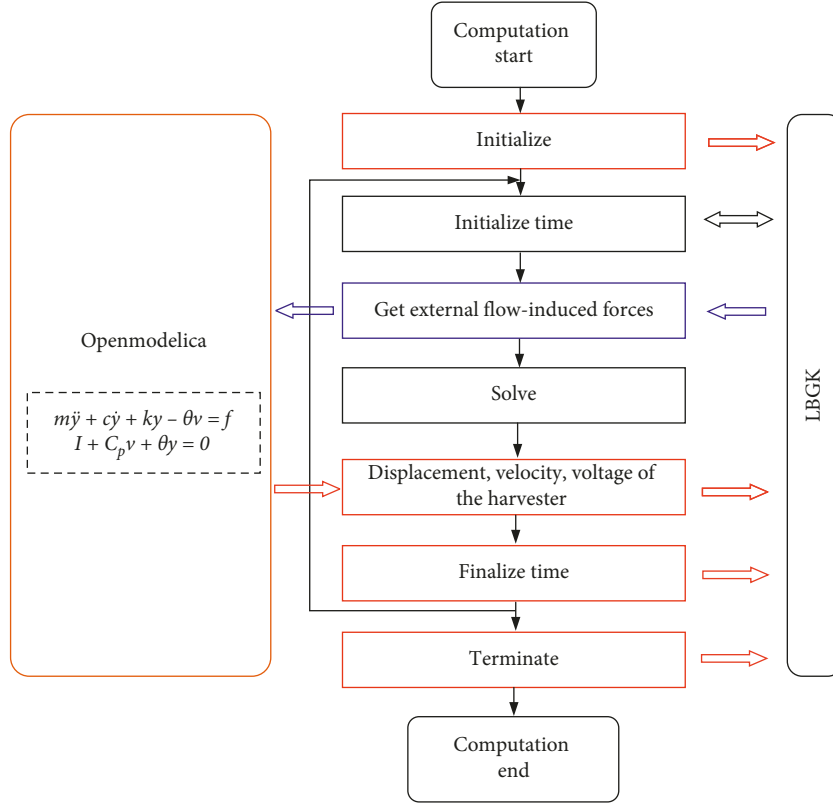


FIGURE 2: The flow chart of the strong coupling computational process.

column that passes over the VIVPEH, a Lattice Boltzmann Method (LBM) is employed to solve the external force on the VIVPEH. Next, by coupling back to the M-C-K equation and the Gauss law, the force connects the flow field and the electromechanical system. Thus, according to the criterion of the equation, one can obtain the vibration amplitude, velocity, accelerated velocity, and voltage output of the system; thus, the signal of vibration amplitude of the VIV bluff body is sent back to the LBM as the initial position of the next timestep.

The updated aerodynamic force obtained by the LBM is sent to the electromechanical coupling system again. The unstable distribution of the flow field and the alternative voltage output the VIVPEH can be available in such an iterative process, which stops if the precision is confirmed.

In this work, the LBM is used to predict the strength of flow-induced vibration of the tandem cylinders in a commercial Xflow code. The advantages of the LBM in solving the fluid-structure interaction problem are as follows: there is no need to solve the Laplace equation at each timestep to satisfy the continuity equation of incompressible, unsteady flows, as is required in solving the Navier–Stokes (NS) equation, and in the LBM, a dynamic mesh is unnecessary in solving the moving boundaries.

The Boltzmann’s transport equation is defined as follows:

$$n_i(\tilde{r} + C_i \Delta t, t + \Delta t) = n_i(\tilde{r}, t) + \Omega^B(n_1, \dots, n_b), \quad (3)$$

where n_i is the statistical distribution functions with real variables, based on the conservation of mass, linear momentum and energy; C_i represents the velocity component

in one of the predetermined direction at discrete time of the particles; and Ω is the collision operator.

By employing a Bhatnagar–Gross–Krook (BGK) approximation, the operator is simplified as

$$\Omega_i^{\text{BGK}} = \frac{1}{\tau} (n_i^{\text{eq}} - n_i), \quad (4)$$

where τ is the relaxation time and n_i^{eq} is the local equilibrium function. For defining the fluid-structure interaction problem, the external force term should be considered, as shown in the following equation:

$$n_i(\tilde{r} + c e_i \Delta t, t + \Delta t) = n_i(\tilde{r}, t) + \Omega_i(n, n^{\text{eq}}) + \Delta t F_i(\tilde{r}, t), \quad (5)$$

where $c = \Delta \tilde{r} / \Delta t$ is the velocity of the particle and F_i is the external force.

4. Verification of the Proposed Mathematical Method

A wind tunnel test is conducted to verify the precision of the simulation code in this work. The experimental setup is shown in Figure 3. The wind is produced by a round wind tunnel, with a diameter of 400 mm. The wind speed is measured by a hot-wire anemometer (Testo Co., USA). The metal substrate is made of pure aluminum, with dimensions of $200 \times 20 \times 0.5 \text{ mm}^3$. An MFC-M2807-P2 (Smart Material Corp, Germany) piezoelectric patch has dimensions of

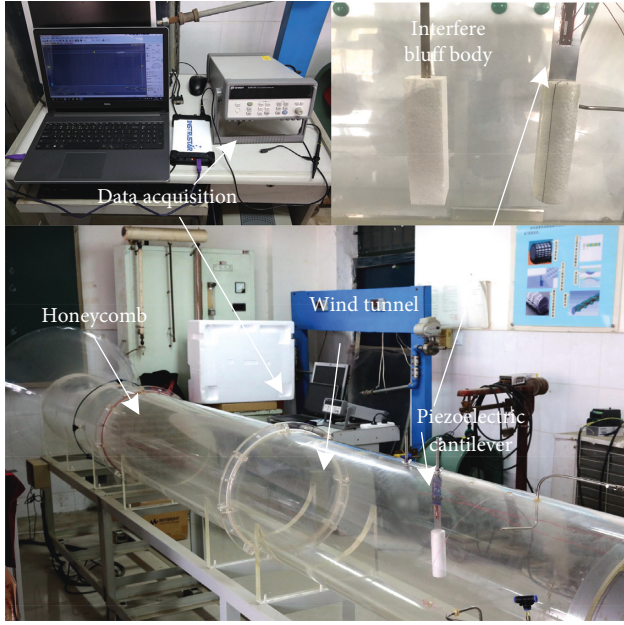


FIGURE 3: Experimental setup.

$37 \times 11 \times 0.3 \text{ mm}^3$. The piezoelectric patch is bound to the root of the cantilever and is connected to an electrical load resistance (R). The voltage output is measured by the NI9221 DAQ module, and the displacement of vibration is measured by a laser displacement sensor (HG-C1400, Panasonic Co., Japan). The stationary square column is also made of foam and is fixed to a wood stick.

The measured parameters of the harvester are listed in Tables 1–3. The wind speed is tested by the hot-wire anemometer and is adjusted by the frequency transducer. Figure 4 shows the relationship between the frequency transducer and the wind speed. To avoid the potential influence of the anemometer, which could act as another bluff body, the fitted line of identifying the wind speed versus the frequency transducer is given based on a substantial amount of measured data.

As shown in Figure 3, a cantilever beam is used as a base layer, and an MFC piezoelectric sheet is bonded to the root of the cantilever beam. This arrangement constitutes a piezoelectric cantilever beam device that is placed at the end of the cantilever beam for generating the vortex-induced vibration.

We compare the results of the voltage output obtained by the CFD simulation with the wind tunnel test to verify the accuracy of the present LBM code. The schematic maps of different lattices are shown in Figures 5(a)–5(c), where L_O is the outside lattice size, L_R is the refining region lattice size, and L_N is the circular cylinder near wall lattice size. Before comparing the predicted results to the experimental results to verify the present simulation code, a lattice independence study was conducted to ensure the accuracy of simulation from. The computational results are shown in Table 4. The lift and drag force coefficients as well as the Strouhal numbers (defined as $S_t = f_s D / U$, f_s is the vortex-shedding frequency) are very close for the lattice numbers of 24000

TABLE 1: Parameters of the piezoelectric cantilever beam.

Properties	Substrate	Piezoelectric transducers
Material	Pure aluminum	MFC
Length	200 mm	37 mm
Width	25 mm	11 mm
Thickness	0.6 mm	0.3 mm
Capacitance	—	15.7 nF

TABLE 2: Parameters of the bluff body.

Properties (bluff body)	Value
Material	Foam
Tip mass	2.28 g
Length (cylinder)	125 mm
Length (square)	125 mm
Diameter	32 mm
Side length	32 mm

TABLE 3: Measured parameters of the M-C-K system.

Properties	Value
M_{eff}	6.59 g
δ	1.083
ξ	0.013
f_n	9.6 Hz
C_{eff}	$0.0098 \text{ N/m}^2 \cdot \text{s}^{-1}$
K_{eff}	34.07 N/m
θ	$1.183 e^{-5} \text{ N/V}$

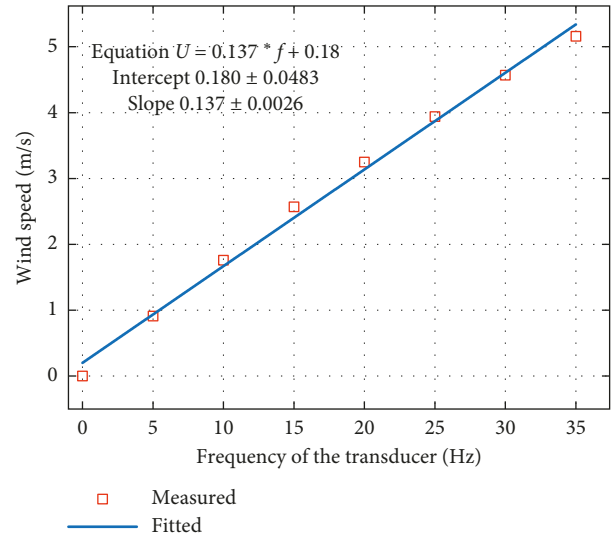


FIGURE 4: The fitted result of the wind speed versus the frequency transducer.

and 53100; thus, the lattice number of 24000 is used in the present work.

The computational results of the voltage output are compared with the experimental results. As shown in Figure 6, the time history results of the present numerical method match well with the experimental results. The FFT results of the voltage output also show good agreement

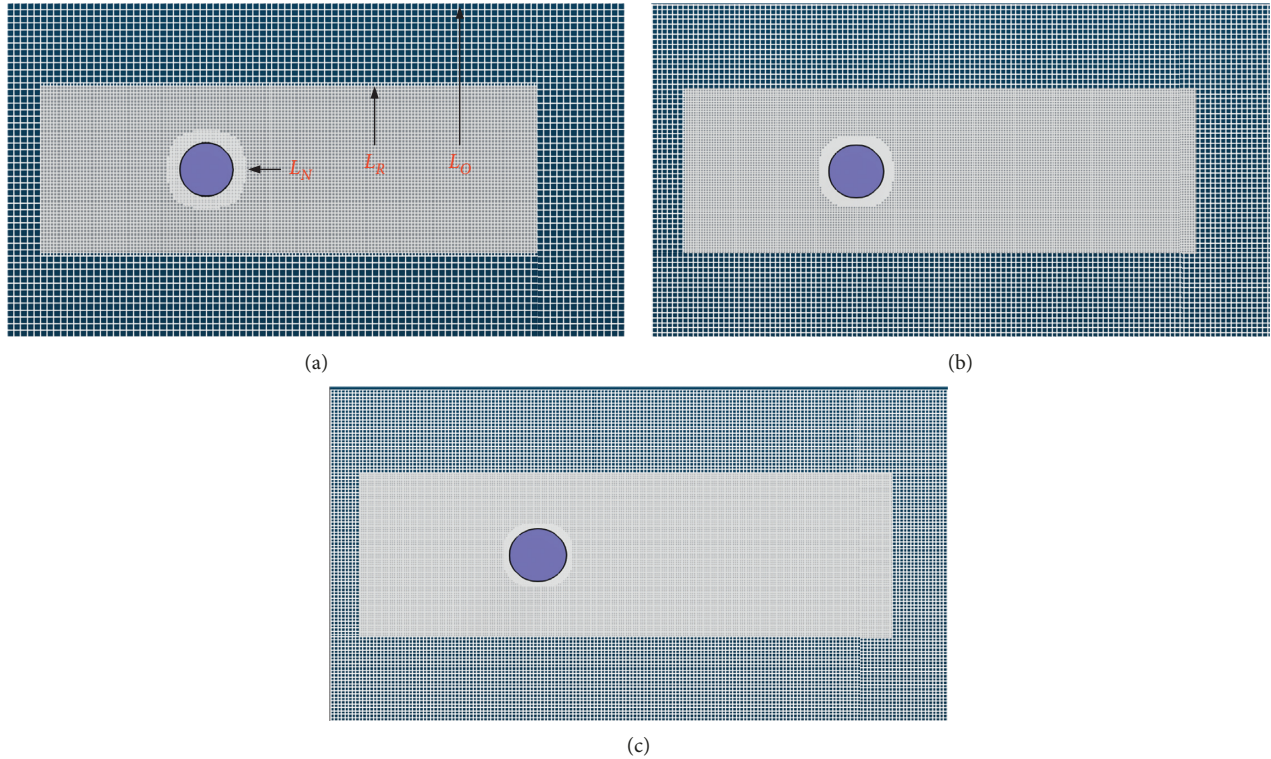


FIGURE 5: Schematic maps of different lattices in the present simulation work.

TABLE 4: Verification of the independence of lattice numbers.

Lattice numbers	Size ($L_O \times L_R \times L_N$)	C_L	C_D	S_t
13990	$0.0004 \times 0.0002 \times 0.0001$	0.533	1.431	0.193
24000	$0.0003 \times 0.00015 \times 0.000075$	0.542	1.422	0.198
53100	$0.0002 \times 0.0001 \times 0.00005$	0.543	1.421	0.199

between the simulation and the experiment; thus, the proposed model is validated.

5. Results and Discussions

First, we conducted the experiments of energy harvesting under different wind speeds. The internal impedance of the data collecting system is equal to $R_L = 1 \text{ M}\Omega$. Figures 7–9 show the time history curves of the voltage output and the fast Fourier transform (FFT) results of the energy harvester under different wind speeds when $l = 1-3L$.

5.1. Voltage Output. As shown in Figures 7(a) and 7(b), for $l = 1L$, in the upper region ($U = 2.78 \text{ m/s}$), there obviously exists two components of vibration, which are the vibration caused by the incoming wind and the Kármán vortex shedding of the forward bluff body. The vibration curve exhibits a “beating”-like phenomenon, i.e., the vibration is dominated by a main frequency, which is the global natural

frequency of the harvester. The maximum voltage output is approximately 15 V. Note that unlike a pure beating phenomenon of a single cylinder vibrating system, because of the influence of the vortex-shedding impact on the upper bluff body, the vortex-shedding frequency of the vibrating circular cylinder is quite chaotic, and the time history curve appears complicated, as shown in Figures 7(a) and 7(b). Figure 7(b) shows that before the resonance occurs, much noise exists in the vortex-shedding frequency of the circular cylinder. When the wind speed increases to 3.56 m/s, the time history curves of the voltage output become more sinusoidal and approach a harmonic response, as shown in Figure 7(c). It is demonstrated that during this stage, the frequency of the vibrating circular cylinder is locked at the global natural frequency. A maximum voltage up to approximately 54.5 V is observed in this stage. Figure 7(d) shows that in the current region, the vibration frequency is quite close to the vortex-shedding frequency of the square column, and the vibration becomes stronger than that shown in Figure 7(a). Figures 7(e) and 7(f) show that when

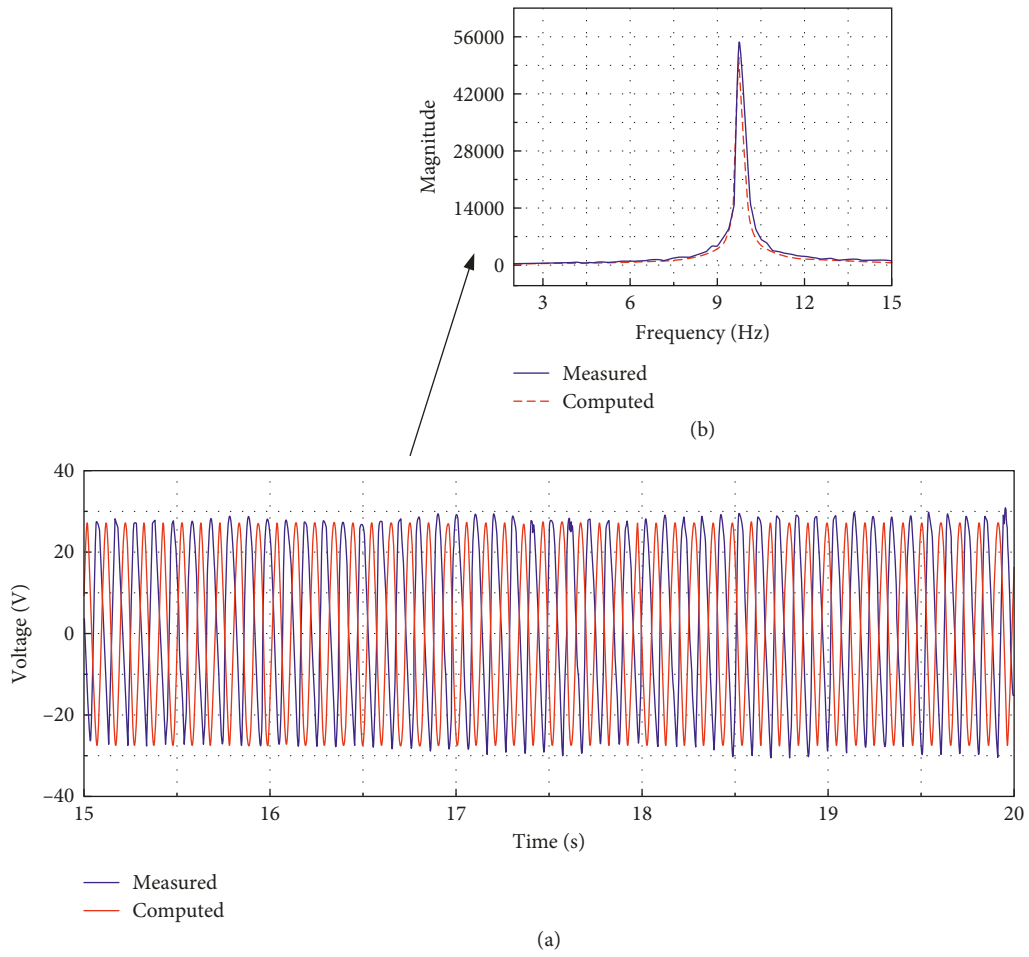


FIGURE 6: Experimental verification of the present numerical work: (a) comparison of the time history curves of the voltage output; (b) comparison of the fast Fourier transformation results of the frequency response for $U = 3.58$ m/s.

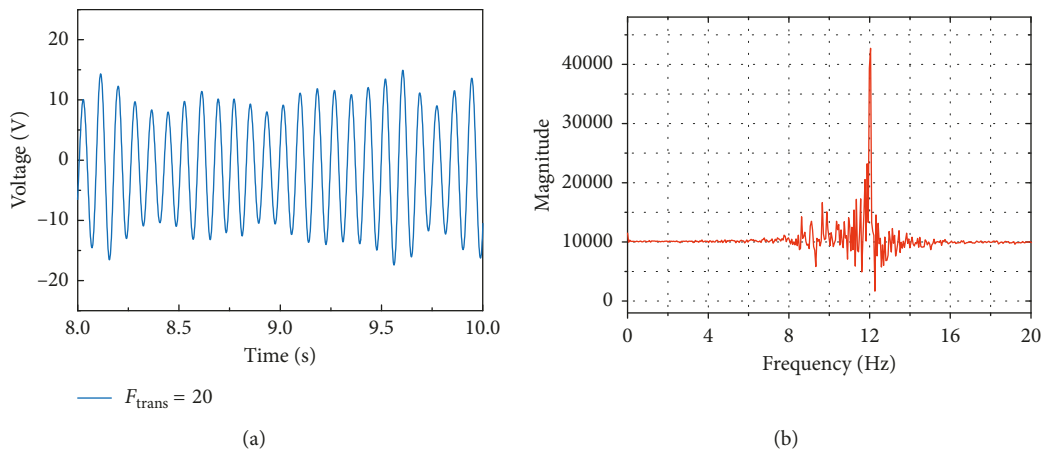


FIGURE 7: Continued.

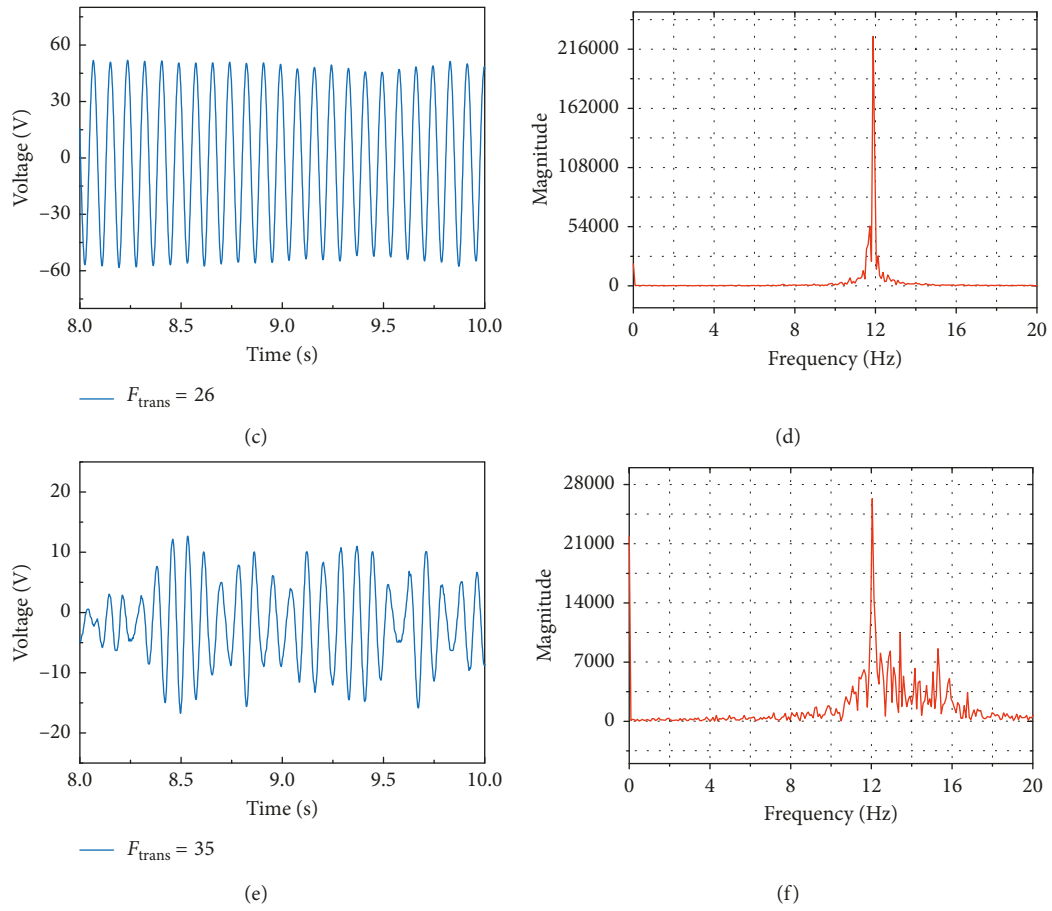


FIGURE 7: Time histories and frequency responses of the voltage outputs for the presynchronous (a, b), synchronous (c, d), and post-synchronous (e, f) regimes of $l = 1L$.

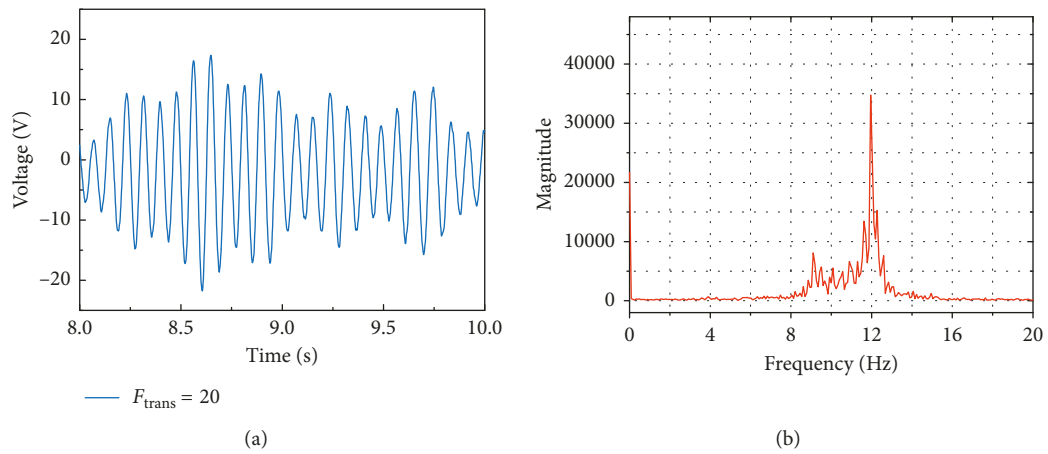


FIGURE 8: Continued.

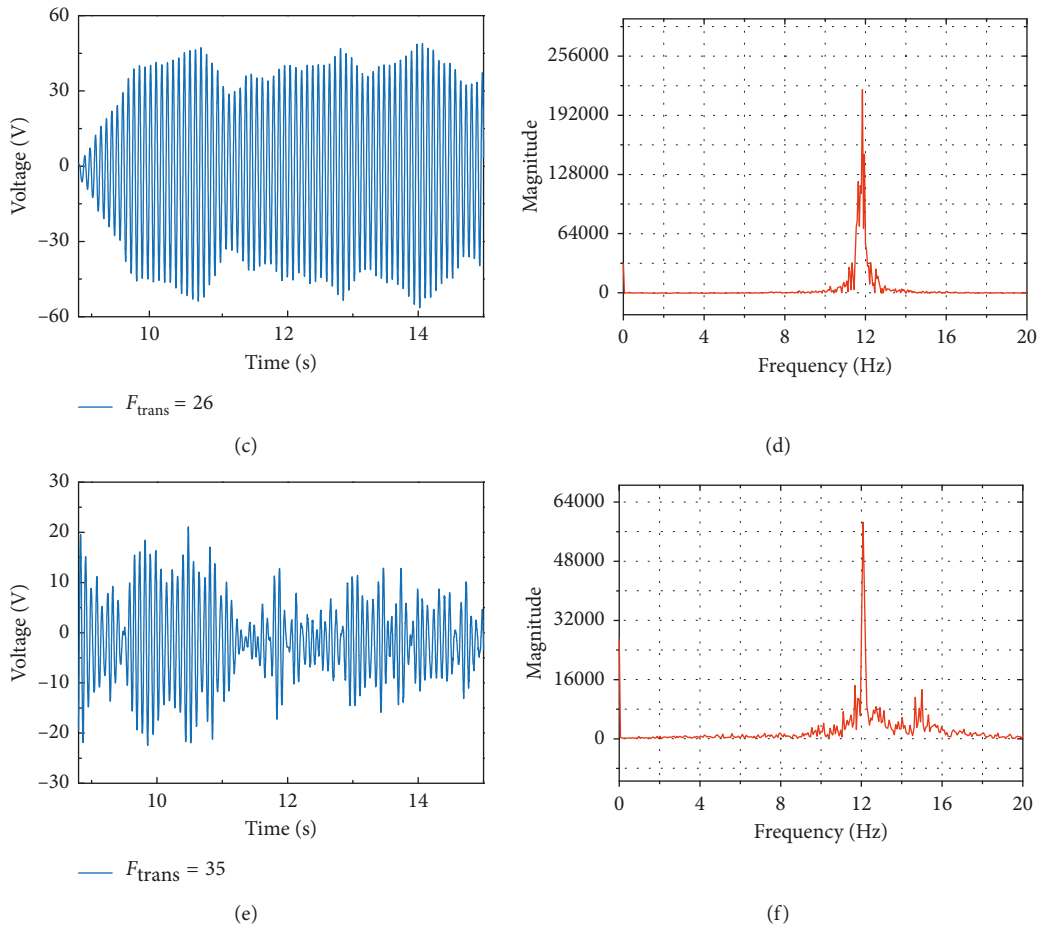


FIGURE 8: Time histories and frequency responses of the voltage outputs for the presynchronous (a, b), synchronous (c, d), and post-synchronous (e, f) regimes of $l = 2L$.

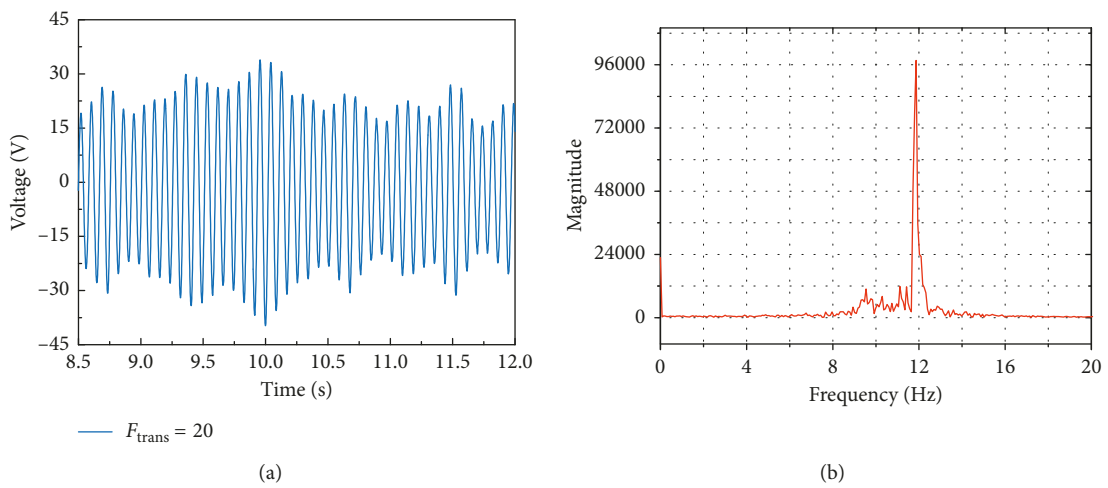


FIGURE 9: Continued.

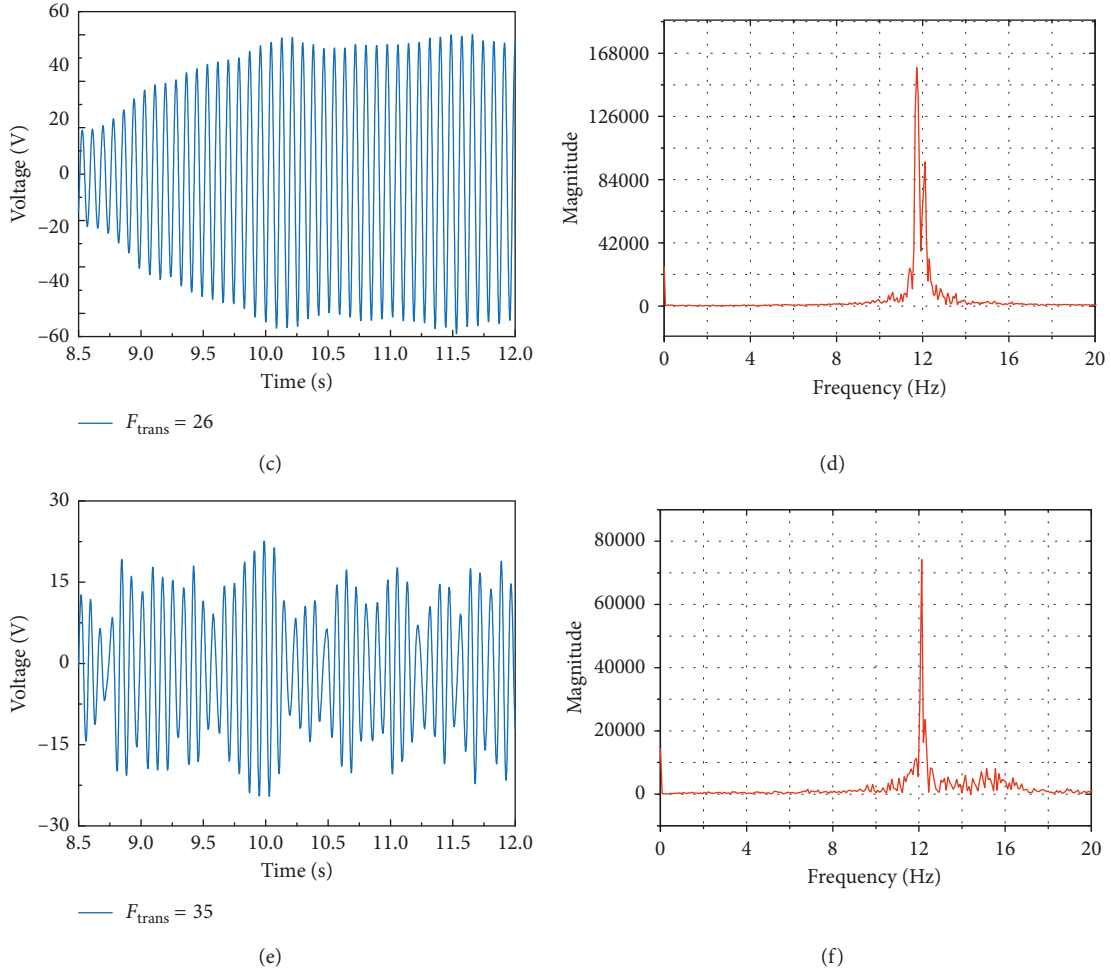


FIGURE 9: Time histories and frequency responses of the voltage outputs for the presynchronous (a, b), synchronous (c, d), and post-synchronous (e, f) regimes of $l=3L$.

the wind speed increases, the vortex-shedding frequency continues to increase and departs from the natural frequency of the circular cylinder; moreover, the vibration amplitudes and the harvested power decrease.

The voltage and frequency response present a similar varying trend for $l=2L$ and $l=3L$. For $l=2L$, the maximum voltage outputs are 24.2 V, 50.5 V, and 23.3 V, respectively, as shown in Figures 8(a), 8(c), and 8(e). The “beating”-like phenomenon occurs again via the combined effects of the vortex and the wake shedding-induced vibration. For $l=3L$, the maximum voltage outputs are 33.8 V, 60.2 V, and 23 V, respectively, as shown in Figures 9(a), 9(c), and 9(e). Moreover, from the FFT results, we can conclude that there exist three different statuses according to the coexistence of the vortex-shedding frequency of the forward cylinder and the global natural frequency of the vibrating cylinder.

Figure 10 compares the influences of wind speed on the voltage output for three different regimes with three harvester configurations. First, unlike the VIV of a single cylinder, one can observe that for different space distances, there is a wind speed range of high amplitude vibration after the VIV lock-in regions. In other words, the circular

cylinder encountered wake-induced buffeting via the wake shedding street of the square column in front. Therefore, the proposed design is able to achieve a considerable enhancement in VIV-based wind energy harvesting. Second, the configuration of $l=3L$ has wider wind speed bandwidth and higher voltage output than the configurations of $l=1L$ and $l=2L$.

Figure 11 shows a comparison of the computed voltage output with the wind tunnel experimental results for $l=3L$. It can be concluded that the predictions and measurements agree well with each other, thus verifying the present simulation method. The discrepancy is mainly attributed to the probabilistic error in the experimental process.

5.2. CFD Computational Results. To clarify the phenomenon of buffeting, as shown in Figure 10, we compared the vortex-shedding patterns in different time regions during a complete vibration period. On the left hand side of Figure 12 ($l=1L$), as shown in Figures 12(a)–12(c), three different regimes of vibration are presented to describe the upper, middle, and lower stages. Figures 12(a)–12(c) also show the peak, the equilibrium, and the valley position of the

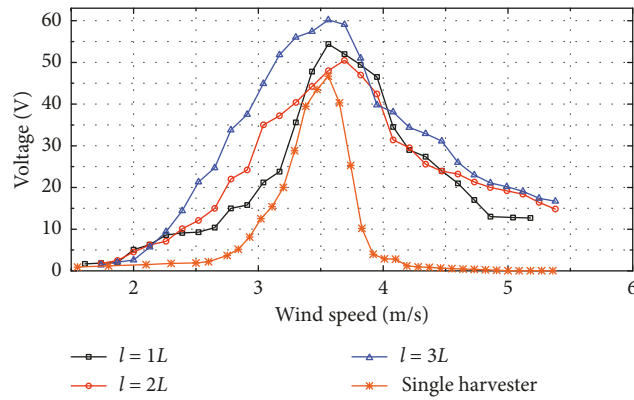


FIGURE 10: Comparisons of the experimental voltage output versus the wind speed of four different regimes. The experimental data from regime-1($l=1L$), regime-2($l=1L$), regime-3($l=1L$) and single harvester are drawn by rectangle, circles, triangle, and stars, respectively.

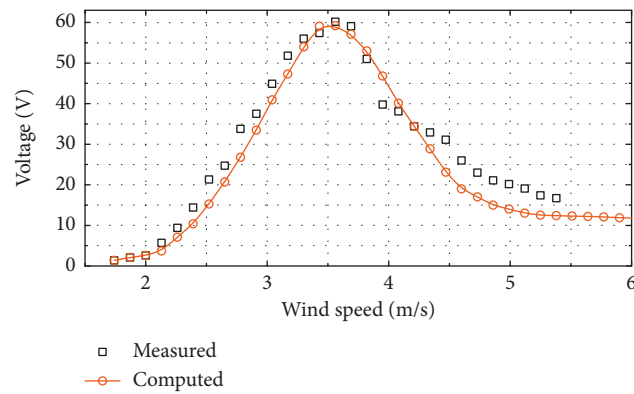


FIGURE 11: Comparisons of the voltage output versus the wind speed between the wind tunnel test and the CFD ($l=3L$).

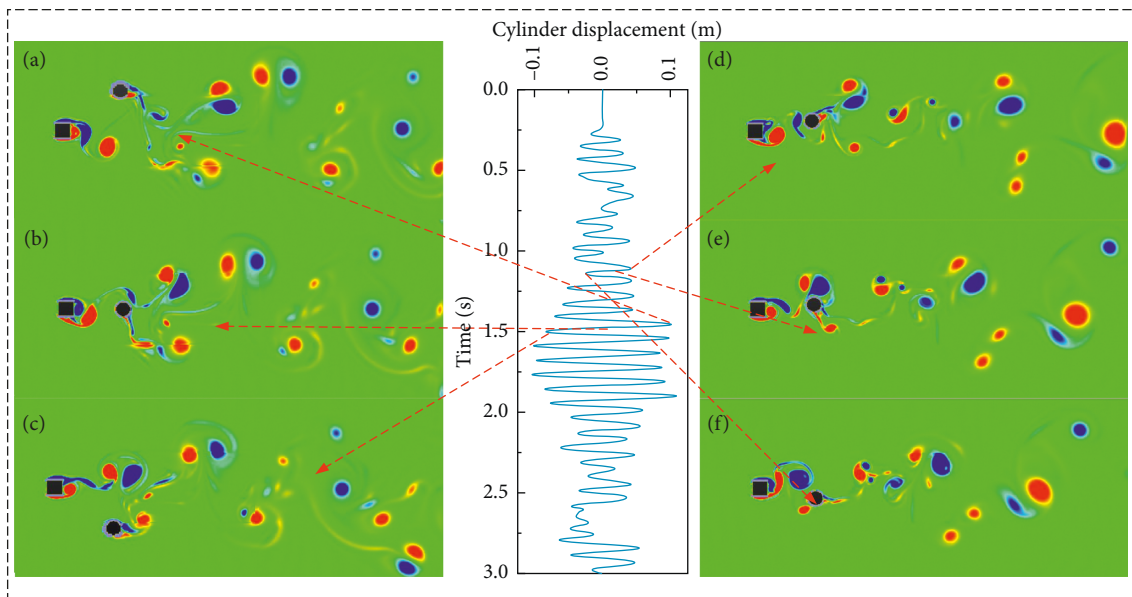


FIGURE 12: Vortex patterns of a complete vibration period ($l=1L$).

vibration during the lock-in part; a “2P + S” pattern mode can be obtained in the current region, in agreement with the results in the literature [36–38]. Figures 12(d)–12(f)

accordingly show the different positions in the wake-induced vibration region on the right hand side. It can be concluded that in this region, the vibration amplitude is much

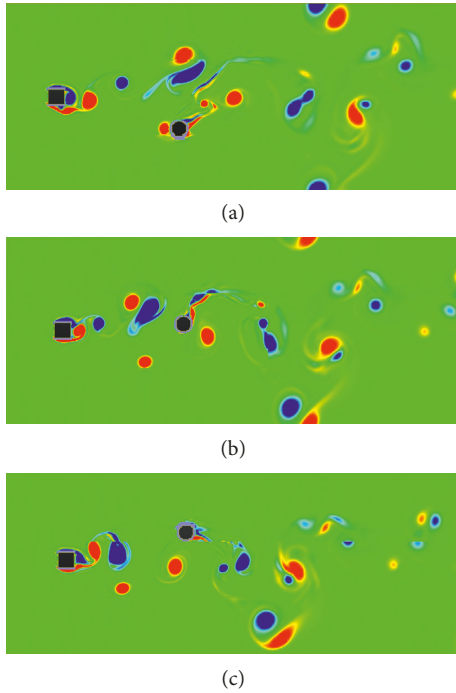


FIGURE 13: Vortex patterns of the high amplitude region ($l=2L$).

lower than that of the lock-in region. Figures 13(a)–13(c) and Figures 14(a)–14(c) present the vortex-shedding patterns in different time regions during a complete vibration period of the lock-in region ($l=2L$ and $l=3L$). The vortex shedding patterns of $l=2L$ and $l=3L$ are close to each other since the space between the stationary square column and the VIV circular cylinder is larger; thus, a typical “P+S” mode is obtained.

6. Conclusions

To enhance the efficiency of flow energy harvesting, higher vibration amplitudes and wider bandwidths are required. In this work, a numerical method combined with the electromechanical coupling model was employed to solve the aero-electromechanical coupling problem of piezoelectric energy harvesting from buffeting. In the proposed approach, the aerodynamic force response from fluid and structure interactions is solved by the LBM method and is then transferred to an electromechanical coupling platform; the vibration position and voltage output are solved and are then sent back to the LBM again as the initial position of the vibration cylinder in the next timestep to obtain the AC voltage time history of the energy harvester and the vibration displacement of the circular cylinder. Three different energy harvester configurations are investigated by varying the space length of the harvester and the interrupting stationary square cylinder. The time histories and the frequency responses of the voltage output are tested in both experiments and numerical simulations; good agreement was found between the experimental results and the simulations. There exist two kinds of frequencies of vibration for the energy harvester according to the VIV and the interrupted vibration

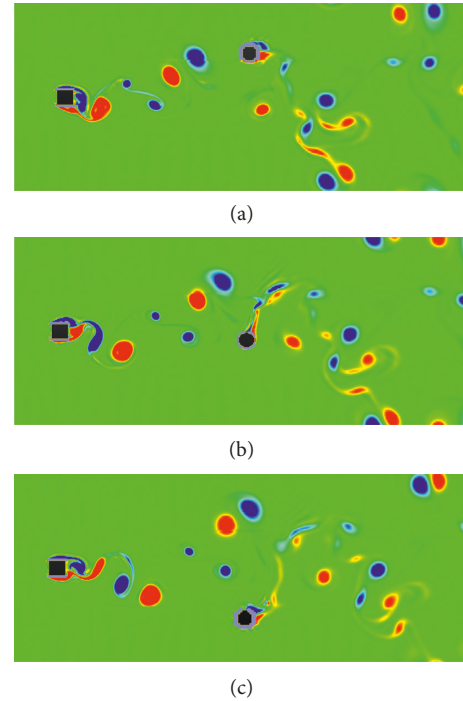


FIGURE 14: Vortex patterns of the high amplitude region ($l=3L$).

influenced by the vortex shedding of the stationary square cylinder. The configuration with $l=3L$ was found to perform better than the other two configurations considered, achieving wider wind speed bandwidth and higher voltage output. The “2P+S” and “P+S” patterns were obtained for $l=1L$ and $l=2-3L$, respectively. Note that for the present energy harvester configurations, unlike the VIVPEH, the vibration could be sustained after the lock-in region. The present phenomenon may enhance the piezoelectric energy harvesting efficiency.

Data Availability

The data used to support the findings of this study are included within the article.

Conflicts of Interest

The authors declare that they have no conflicts of interest.

Acknowledgments

The authors gratefully acknowledge the support provided by the National Natural Science Foundation of China (nos. 51606171, 51578512, 51108425, and 51705469), the China Postdoctoral Science Foundation (no. 2017M612417), and the Science and Technology Research Program of Chongqing Municipal Education Commission (Grant no. KJ1705142).

References

- [1] K. Tao, L. Tang, J. Wu, W. L. Sun, H. Chang, and J. Miao, “Investigation of multimodal electret-based MEMS energy

- harvester with impact-induced nonlinearity,” *Journal of Microelectromechanical Systems*, vol. 27, no. 2, pp. 276–288, 2018.
- [2] S. X. Zhou, J. Y. Cao, G. Litak, and J. Lin, “Numerical analysis and experimental verification of broadband tristable energy harvesters,” *tm—Technisches Messen*, vol. 85, no. 9, pp. 521–532, 2018.
 - [3] L. Y. Zhao, L. H. Tang, J. R. Liang, and Y. W. Yang, “Synergy of wind energy harvesting and synchronized switch harvesting interface circuit,” *IEEE/ASME Transactions on Mechatronics*, vol. 22, no. 2, pp. 1093–1103, 2017.
 - [4] B. Zhang, B. Ducharme, B. Gupta et al., “Experimental sea wave energy extractor based on piezoelectric Ericsson cycles,” *Journal of Intelligent Material Systems & Structures*, vol. 29, no. 6, pp. 1102–1112, 2017.
 - [5] X. Q. Zhao, Z. G. Shang, G. X. Luo, and L. C. Deng, “A vibration energy harvester using AlN piezoelectric cantilever array,” *Microelectronic Engineering*, vol. 142, pp. 47–51, 2015.
 - [6] N. Shao, J. J. Lian, G. B. Xu et al., “Experimental investigation of flow-induced motion and energy conversion of a T-section prism,” *Energies*, vol. 11, no. 8, p. 2035, 2018.
 - [7] S. X. Zhou and L. Zuo, “Nonlinear dynamic analysis of asymmetric tristable energy harvesters for enhanced energy harvesting,” *Communications in Nonlinear Science and Numerical Simulation*, vol. 61, pp. 271–284, 2018.
 - [8] S. X. Zhou and J. L. Wang, “Dual serial vortex-induced energy harvesting system for enhanced energy harvesting,” *AIP Advances*, vol. 8, no. 7, article 075221, 2018.
 - [9] K. Q. Fan, Q. X. Tan, H. Y. Liu, Y. M. Zhu, W. D. Wang, and D. X. Zhang, “Hybrid piezoelectric-electromagnetic energy harvester for scavenging energy from low-frequency excitations,” *Smart Materials & Structures*, vol. 27, article 085001, 2018.
 - [10] Y. P. Wu, H. L. Ji, J. H. Qiu, W. Q. Liu, and J. L. Zhao, “An internal resonance based frequency up-converting energy harvester,” *Journal of Intelligent Material Systems & Structures*, vol. 29, no. 13, pp. 2766–2781, 2018.
 - [11] J. L. Wang, G. F. Zhao, M. Zhang, and Z. E. Zhang, “Efficient study of a coarse structure number on the bluff body during the harvesting of wind energy,” *Energy Sources Part A-Recovery Utilization and Environmental Effects*, vol. 40, no. 15, pp. 1788–1797, 2018.
 - [12] Y. Zhang, L. H. Tang, and K. F. Liu, “Piezoelectric energy harvesting with a nonlinear energy sink,” *Journal of Intelligent Material Systems and Structures*, vol. 28, no. 3, pp. 307–322, 2017.
 - [13] M. Bryant and E. Garcia, “Energy harvesting: a key to wireless sensor nodes,” in *Proceedings of Second International Conference on Smart Materials and Nanotechnology in Engineering*, p. 74931W, International Society for Optics and Photonics, Weihai, China, October 2009.
 - [14] A. I. Aquino, J. K. Calautit, and B. R. Hughes, “Evaluation of the integration of the Wind-Induced Flutter Energy Harvester (WIFEH) into the built environment: experimental and numerical analysis,” *Applied Energy*, vol. 207, pp. 61–77, 2017.
 - [15] F. Ewere, G. Wang, and A. Frendi, “Experimental investigation of a bioinspired bluff-body effect on galloping piezoelectric energy-harvester performance,” *AIAA Journal*, vol. 56, no. 3, pp. 1284–1287, 2018.
 - [16] Y. W. Yang, L. Y. Zhao, and L. H. Tang, “Comparative study of tip cross-sections for efficient galloping energy harvesting,” *Applied Physics Letters*, vol. 102, no. 6, article 064105, 2013.
 - [17] L. A. Weinstein, M. R. Cacan, P. So, and P. Wright, “Vortex shedding induced energy harvesting from piezoelectric materials in heating, ventilation and air conditioning flows,” *Smart Materials and Structures*, vol. 21, no. 4, article 045003, 2012.
 - [18] M. Zhang, G. F. Zhao, and J. L. Wang, “Study on fluid-induced vibration power harvesting of square columns under different attack angles,” *Geofluids*, vol. 2017, Article ID 6439401, 18 pages, 2017.
 - [19] H. L. Dai, A. Abdelkefi, Y. W. Yang, and L. Wang, “Orientation of bluff body for designing efficient energy harvesters from vortex-induced vibrations,” *Applied Physics Letters*, vol. 108, no. 5, article 053902, 2016.
 - [20] J. Hobeck and D. Inman, “Dual cantilever flutter: experimentally validated lumped parameter modeling and numerical characterization,” *Journal of Fluids and Structures*, vol. 61, pp. 324–338, 2016.
 - [21] R. J. Connor, S. H. Collicott, A. M. Deschepper, R. J. Sherman, A. J. Ocampo, and A. Medicine, *Fatigue Loading and Design Methodology for High-Mast Lighting Towers*, The National Academies Press, Washington, DC, United States, 2012.
 - [22] M. P. Paidoussis, S. J. Price, and E. De Langre, *Fluid-structure interactions: cross-flow-induced instabilities*, Cambridge University Press, Cambridge, UK, 2010.
 - [23] J. C. Liao and M. S. Triantafyllou, “Fish exploiting vortices decrease muscle activity,” *Science*, vol. 302, no. 5650, pp. 1566–1569, 2003.
 - [24] D. Beal, F. Hover, M. Triantafyllou, J. Liao, and G. Lauder, “Passive propulsion in vortex wakes,” *Journal of Fluid Mechanics*, vol. 549, no. 1, pp. 385–402, 2006.
 - [25] J. J. Allen and A. J. Smits, “Energy harvesting Eel,” *Journal of Fluids and Structures*, vol. 15, no. 3–4, pp. 629–640, 2001.
 - [26] H. D. Akaydin, N. Elvin, and Y. Andreopoulos, “The performance of a self-excited fluidic energy harvester,” *Smart Materials and Structures*, vol. 21, no. 2, article 025007, 2012.
 - [27] O. Goushcha, N. Elvin, and Y. Andreopoulos, “Interactions of vortices with a flexible beam with applications in fluidic energy harvesting,” *Applied Physics Letters*, vol. 104, no. 2, article 021919, 2014.
 - [28] A. Erturk and D. J. Inman, “A distributed parameter electromechanical model for cantilevered piezoelectric energy harvesters,” *Journal of Vibration and Acoustics*, vol. 130, no. 4, article 041002, 2008.
 - [29] R. E. D. Bishop and A. Hassan, “The lift and drag forces on a circular cylinder in a flowing fluid,” *Proceedings of the Royal Society A: Mathematical, Physical and Engineering Sciences*, vol. 277, no. 1368, pp. 32–50, 1964.
 - [30] R. T. Hartlen and I. G. Currie, “Lift-oscillator model of vortex-induced vibration,” *Journal of the Engineering Mechanics Division*, vol. 96, no. 5, pp. 577–591, 1970.
 - [31] O. Griffin, R. Skop, and G. Koopmann, “The vortex-excited resonant vibrations of circular cylinders,” *Journal of Sound and Vibration*, vol. 31, no. 2, pp. 235–IN3, 1973.
 - [32] R. Skop and O. Griffin, “A model for the vortex-excited resonant response of bluff cylinders,” *Journal of Sound and Vibration*, vol. 27, no. 2, pp. 225–233, 1973.
 - [33] A. H. Nayfeh, *Introduction to Perturbation Techniques*, John Wiley & Sons, Hoboken, NJ, USA, 2011.
 - [34] M. L. Facchinetti, E. De Langre, and F. Biolley, “Coupling of structure and wake oscillators in vortex-induced vibrations,” *Journal of Fluids and structures*, vol. 19, no. 2, pp. 123–140, 2004.
 - [35] A. Farshidianfar and H. Zanganeh, “A modified wake oscillator model for vortex-induced vibration of circular cylinders

- for a wide range of mass-damping ratio,” *Journal of Fluids and Structures*, vol. 26, no. 3, pp. 430–441, 2010.
- [36] S. Bao, S. Chen, Z. Liu, J. Li, H. Wang, and C. Zheng, “Simulation of the flow around an upstream transversely oscillating cylinder and a stationary cylinder in tandem,” *Physics of Fluids*, vol. 24, no. 2, p. 197, 2012.
- [37] Y. Bao, D. Zhou, and J. Tu, “Flow interference between a stationary cylinder and an elastically mounted cylinder arranged in proximity,” *Journal of Fluids & Structures*, vol. 27, no. 8, pp. 1425–1446, 2011.
- [38] Z. Han, D. Zhou, and J. Tu, “Wake-induced vibrations of a circular cylinder behind a stationary square cylinder using a semi-implicit characteristic-based split scheme,” *Journal of Engineering Mechanics*, vol. 140, no. 8, article 04014059, 2014.

